Digital in-line holographic microscopy

Jorge Garcia-Sucerquia, Wenbo Xu, Stephan K. Jericho, Peter Klages, Manfred H. Jericho, and H. Jürgen Kreuzer

We first briefly review the state of the art of digital in-line holographic microscopy (DIHM) with numerical reconstruction and then discuss some technical issues, such as lateral and depth resolution, depth of field, twin image, four-dimensional tracking, and reconstruction algorithm. We then present a host of examples from microfluidics and biology of tracking the motion of spheres, algae, and bacteria. Finally, we introduce an underwater version of DIHM that is suitable for *in situ* studies in an ocean environment that show the motion of various plankton species. © 2006 Optical Society of America

OCIS codes: 090.0090, 090.1760, 180.6900, 110.0180, 100.2000, 100.6640.

1. Introduction

Over 50 years ago, Gabor[1] proposed a new principle of microscopy to overcome the limitations of lenses, particularly those of electric and magnetic lenses in electron microscopy. In-line holography with spherical waves, as originally proposed by Gabor, is the simplest realization of the holographic method, working without lenses. Its applications have been limited, however, until recently owing to the fact that reconstruction of the object image with another wave (light or electron) is not practical. To avoid this problem, researchers have developed various schemes of off-line holography.[2–6] Another option, which was already contemplated by Gabor, is numerical reconstruction.[7–12]

In-line holography with electrons was revived in the late 1980s by Fink,[13,14] Stocker *et al.*,[15] and Fink *et al.*[16,17] when they managed to make stable field-emission tips that ended in a single atom, thus creating an intense point source for coherent electrons in the energy range from roughly 10 to 300 eV, i.e., for wavelengths from 2 to 0.5 Å. High-resolution holograms were recorded digitally by using a CCD camera, and a theory was developed for the numerical reconstruction of these holograms.[18,19] These must be considered the first successes of digital in-line holography with electrons.[20–23] Although the reconstruction algorithm was originally designed for electron holography, its transfer to optical holography is straightforward.[24–27]

The feasibility and advantages of numerical reconstruction of digitally recorded holograms gave rise to several new holographic techniques to study micrometer-sized three-dimensional (3-D) phenomena. By taking advantage of the phase information, one can determine the contour of the nanometric structures.[28] Using a combination of different wavelengths allows one to enlarge the range of application of the phase-based methods.[29] Applying phase-shifting techniques makes it possible to get rid of the twin-image noise present in many holographic reconstructions of macrosized and microsized objects.[30–32] Another powerful technique to enhance 3-D resolution is optical scanning holography, a method that can also be adapted to cryptography.[33–37] All these techniques require sophisticated optical setups far beyond the simplicity of the in-line geometry.

Digital in-line holographic microscopy (DIHM) was recently developed as a new tool that yields 3-D images of objects with micrometer resolution, such as microspheres,[27,38] cells, plankton, and other biological specimens.[39] In addition, a technique was designed that allows the study of moving objects, giving images of their 3-D trajectories that represent the flow in microfluidics, the motion of plankton in water, the motion of bacteria in cells, and much more.[40–45] Because the in-line holographic microscope is so simple and so sturdy, an underwater version has been developed that has produced images of swimming plankton in the ocean environment.

This paper is organized as follows. In Section 2 we

J. Garcia-Sucerquia (jigarcia@Fizz.Phys.Dal.Ca), W. Xu, S. K. Jericho, P. Klages, M. H. Jericho, and H. J. Kreuzer are with the Department of Physics and Atmospheric Science, Dalhousie University, Halifax, Nova Scotia B3H 3J5, Canada. J. Garcia-Sucerquia is also with the Physics School, Universidad Nacional de Colombia Sede Medellin, Apartado Aéreo 3840. Medellin, Colombia.

Received 16 May 2005; revised 16 August 2005; accepted 16 August 2005.

0003-6935/06/050836-15$15.00/0

© 2006 Optical Society of America

begin with some technical details about DIHM, particularly about the reconstruction algorithm, four-dimensional (4-D) tracking, resolution, and depth of field. We derive criteria for the lateral and depth resolution limits in DIHM, which we validate with numerical modeling and experimental results. Those results show without ambiguity that a resolution of the order of a wavelength can be easily reached with DIHM. We also provide experimental evidence that the twin image is not a problem in DIHM. In Section 3 we present a host of applications of DIHM in microfluidics, cell biology, and marine biology, with the latter obtained with an underwater version of DIHM. The paper concludes with a summary and a look to the future.

2. Digital In-Line Holographic Microscopy: Technical Details

A. Contrast Image and Reconstruction

In in-line holography a spherical wave of wavelength λ, emanating from a point source of linear dimensions of the order of a wavelength, illuminates an object, typically a distance of a few thousand wavelengths from the source, and forms a highly magnified diffraction pattern on a screen much farther away (see Fig. 1).

We denote by $A(\mathbf{r}, t)$ the wave amplitude (the wave function for electrons and the electric field vector or scalar field for photons) and split it into the unscattered reference wave, $A_{\mathrm{ref}}(\mathbf{r}, t)$, and the wave, $A_{\mathrm{scat}}(\mathbf{r}, t)$, scattered by the object. Ideally the reference wave emanating from the source is a spherical wave, $A_{\mathrm{ref}}(\mathbf{r}, t) = \exp(ikr)/r$, where $k = 2\pi/\lambda$ is the wavenumber. In an experiment this spherical wave is modified by the emission cone of the source. However, this can, at least in part, be corrected by constructing from the intensity, $|A(\mathbf{r}, t)|^2$, the contrast image as follows:

$$\begin{aligned}\tilde{I}(\mathbf{r},\, t) &= |A_{\mathrm{ref}}(\mathbf{r},\, t) + A_{\mathrm{scat}}(\mathbf{r},\, t)|^2 - |A_{\mathrm{ref}}(\mathbf{r},\, t)|^2 \\ &= [A_{\mathrm{ref}}{}^*(\mathbf{r},\, t)A_{\mathrm{scat}}(\mathbf{r},\, t) + A_{\mathrm{ref}}(\mathbf{r},\, t)A_{\mathrm{scat}}{}^*(\mathbf{r},\, t)] \\ &\quad + |A_{\mathrm{scat}}(\mathbf{r},\, t)|^2. \end{aligned} \tag{1}$$

We refer to the first term (in brackets in the second line) in Eq. (1), linear in the scattered wave, as the holographic diffraction pattern because it arises from the superposition of the interference terms between the unscattered reference wave from the source and the scattered wave from the object. The second term in Eq. (1) contains the interference between the scattered waves. We refer to it as the classical diffraction pattern. Holographic diffraction dominates the images for small objects; loosely speaking, small means that the object should block only a fraction of the cone of radiation recorded on the screen. Even if these objects are opaque, we are still in the regime of holography and will be able to recover the outline or shape of the object by reconstruction. Because more of the incoming reference wave is blocked by larger objects the scattered wave amplitude grows, and classical diffraction eventually dominates the image, placing us in the regime of classical wave optics.

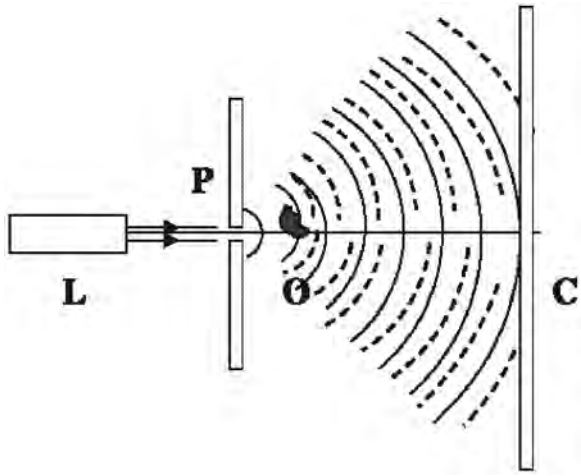

Fig. 1. Schematic of DIHM: laser L is focused onto pinhole P. The emerging spherical wave illuminates object O, and the interference pattern or hologram is recorded on screen C.

Holography is a two-step process: First, a hologram must be recorded, and second, reconstruction must yield an image of the object, i.e., the intensity of the wavefront at the object. In DIHM the hologram is recorded by a detector array, such as a multichannel plate for electrons or a CCD camera for photons, and is transferred to a computer in which the reconstruction is performed numerically. The role of reconstruction is to obtain the 3-D structure of the object from the two-dimensional (2-D) hologram on the screen or, in physical terms, to reconstruct the wavefront at the object. This can be achieved via a Kirchhoff–Helmholtz transform[18,46–48]:

$$K(\mathbf{r}) = \int_{\mathrm{screen}} \mathrm{d}^2\xi\, \tilde{I}(\boldsymbol{\xi}) \exp[ik\mathbf{r}\cdot\boldsymbol{\xi}/|\boldsymbol{\xi}|], \tag{2}$$

in which the integration extends over the 2-D surface of the screen with coordinates $\xi = (X, Y, L)$, where L is the distance from the source (pinhole) to the center of the screen (CCD chip) and $\tilde{I}(\boldsymbol{\xi})$ is the contrast image (hologram) on the screen obtained by subtracting the images with and without the object present. The function $K(\mathbf{r})$ is significantly structured and different from zero only in the space region occupied by the object. By reconstructing the wavefront $K(\mathbf{r})$ on a number of planes at various distances from the source in the vicinity of the object, a 3-D image can be built up from a single 2-D hologram. Here $K(\mathbf{r})$ is a complex function, and one usually plots the intensity $|K(\mathbf{r})|^2$ to represent the object, although phase images are also available. For the numerical implementation of the transform, a fast algorithm was developed that evaluates $K(\mathbf{r})$ without any approximations.[19] The algorithm employs a coordinate transformation to remove the nonlinearity in the exponential that transforms the integral into a convo-

lution, which is solved by three consecutive 2-D fast Fourier transforms (FFT), providing a choice of the size of the reconstructed image so that one can magnify different parts of the object at will. We should stress that simplifying the Helmholtz–Kirchhoff transform by an on-axis approximation, $\xi = (X^2 + Y^2 + L^2)^{1/2} = L$, and solving it by a single 2-D FFT eliminates this choice because it automatically fixes the linear size of the pixel in the reconstructed image to be $\delta = \lambda L/(N\Delta)$ in terms of the wavelength λ, distance L from the point source to the screen, and the dimension of the recording screen (CCD chip), $N\Delta \times N\Delta$. Although it is widely used,[49–51] the on-axis approximation is valid only for small numerical apertures, which in itself of course limits the resolution of the microscope. Moreover, compared with the on-axis approximation, our fast algorithm is numerically as expedient and yields much superior images, as we demonstrate below.

In holography the term reconstruction is used to obtain the function $K(\mathbf{r})$ from the hologram. The plot of $|K(\mathbf{r})|^2$ on a 2-D plane, which we call a 2-D holographic reconstruction, is equivalent to one in-focus image taken in a conventional compound microscope. In DIHM one can generate a stack of 2-D holographic reconstructions from a single hologram. Combining such a stack will result in a 3-D image of the object; this latter step is usually referred to as 3-D reconstruction or 3-D rendering.

As an aside, we should briefly comment on the intensities in DIHM reconstructions. In a bright field image of a compound microscope, in which the background is light, transparent objects are bright and opaque objects are dark. In contrast, the background in the holographic reconstruction is dark because we used a contrast hologram from which the bright background is subtracted. Any objects, transparent or opaque, are lighter than the background because both are the origin of scattered waves that we have traced back from the hologram in the reconstruction. After all, the contrast image from which the reconstruction is obtained is identically zero in the absence of an object leading to a uniformly black reconstructed image. Because an opaque sphere absorbs more of the incoming light, it is less bright than a transparent sphere.

The experimental setup for DIHM, following the schematic of Fig. 1, is simple: A laser is directed onto a pinhole of a diameter of the order of a wavelength, which acts as the point source from which a spherical wave of wavelength λ emanates. The wave illuminates an object (in our setup located a few millimetres from the pinhole) and forms a geometrically magnified diffraction pattern on a screen, in our case a CCD chip, about a centimeter away. The hologram is stored as a digital image in a computer for reconstruction.

B. Four-Dimensional Imaging

The efficient recording of the trajectories of objects that are moving throughout a 3-D space has been a big problem in several branches of science such as colloidal suspensions, the motion of algae or larvae in water, the motion of bacteria around and in cells, and the characterization of marine particulates. Because of its large depth of field, DIHM is ideally suited for capturing the 3-D motion of many objects (algae, plankton, beads, etc.) with temporal and spatial resolution at the subsecond and micrometer level.

To obtain high-resolution DIHM reconstruction images of the trajectories of the objects in a tank, we proposed the following procedure[42]:

(i) A sequence of holograms (h_i) is recorded by a CCD camera with a sufficiently high capture rate and is transferred to a computer.

(ii) The undesired background effects are eliminated by subtracting consecutive hologram pairs, pixel by pixel, to generate new holograms, i.e., $(h_1 - h_2)$, $(h_3 - h_4)$, etc.

(iii) The resultant difference pictures are summed (a few hundred holograms could be combined) into a single file, which now contains all holograms (albeit with alternate sign), yet it has the same size as any single original hologram. Subtracting alternate holograms ensures that the dynamic range is not exceeded and that only the object-related information (moving algae, for example) is retained.

(iv) The combined file, called the difference hologram, is then reconstructed with the Kirchhoff–Helmholtz transform [Eq. (2)] to obtain images at different depth planes in the sample volume. A stack of such images shows the sequential positions at successive recording times of the objects contained in the sample volume, and the vectors connecting two successive positions define the velocity field; this is particularly impressive in a 3-D rendering.

We emphasize the efficiency of the data collection in our procedure. The removal of background effects and the construction of summed holograms are easily accomplished so that high-resolution 4-D tracking of many particles from just a single hologram data set can be performed. Since resolutions of the order of a wavelength of light were achieved with DIHM, tracking organisms as small as bacteria is possible, as would be the motion of plankton in water or, at lower resolution, the aerial trajectories of flying insects. Outside biology, applications of 4-D DIHM are possible in particle velocimetry, i.e., tracking the motion of particles in a liquid or in gas flows, visualization of structures in convective or turbulent flow and in colloidal suspensions, remote sensing and environmental monitoring, and investigation of bacterial attachment to surfaces and biofilm formation to name but a few.

C. Resolution and Depth of Field in Digital In-Line Holographic Microscopy

Resolution in DIHM depends on several controllable factors or parameters: (1) pinhole size, controlling spatial coherence and illumination cone; (2) numerical aperture, given by the size and positioning of the recording CCD chip; (3) pixel density and

dynamic range, controlling fringe resolution and noise level in the hologram; and (4) wavelength. We present a detailed study of the individual and combined effects of these factors by conducting an analytical analysis coupled with numerical simulations of holograms and their reconstruction. The result of this analysis is a set of criteria that can be used for the optimum design of the DIHM setup. We also present a series of experimental results that test and confirm our theoretical analysis. The ultimate resolution to date is the imaging of the motion of spheres, bubbles, and bacteria that are ~1 μm in size, a few micrometers apart, and moving at speeds of ~100 μm/s.

1. Model Calculations

To study the problem of resolution in DIHM, we use a model that is tailored to suit the Rayleigh and Sparrow criteria[52–54] for resolution, which state (Rayleigh) that two point sources are just resolved when the principal intensity maximum of one coincides with the first intensity minimum of the other or (Sparrow) for unequal source intensities when the first and second derivatives of the intensity with respect to the line connecting the two points vanish. In the case of DIHM, these criteria are applicable to the reconstructed images, and the question remains of what kind of conditions they impose on the underlying holograms from which the reconstructions were performed. Simply put, we need to know how many interference fringes must be captured and in what detail to ensure that the Rayleigh and Sparrow criteria are met in reconstruction.

The model for DIHM consists of an ideal point source that emits a spherical wave $A_{\mathrm{ref}}(\mathbf{r}) = A_0 r^{-1} \exp[ikr]$ with wavenumber $k = 2\pi/\lambda$. In addition, we have two objects, also modeled as point sources, at positions $\mathbf{r}_1$ and $\mathbf{r}_2$, from which scattered spherical waves emerge. The total wave field is thus

$$A(\mathbf{r}) = A_0 \frac{\exp[ikr]}{r} + A_1 \frac{\exp[ik|\mathbf{r}-\mathbf{r}_1|]}{|\mathbf{r}-\mathbf{r}_1|} + A_2 \frac{\exp[ik|\mathbf{r}-\mathbf{r}_2|]}{|\mathbf{r}-\mathbf{r}_2|}. \tag{3}$$

The intensity of the contrast image then becomes

$$\begin{aligned}\tilde{I}(\mathbf{r}) &= I(\mathbf{r}) - \frac{{A_0}^2}{r^2} \\ &= \frac{{A_1}^2}{|\mathbf{r}-\mathbf{r}_1|^2} + \frac{{A_2}^2}{|\mathbf{r}-\mathbf{r}_2|^2} \\ &\quad + 2\frac{A_1 A_2}{|\mathbf{r}_1-\mathbf{r}_2|^2}\cos[k(|\mathbf{r}-\mathbf{r}_1| - |\mathbf{r}-\mathbf{r}_2|)] \\ &\quad + \left\{2\frac{A_0 A_1}{r|\mathbf{r}-\mathbf{r}_1|}\cos[k(r-|\mathbf{r}-\mathbf{r}_1|)]\right. \\ &\quad \left. + 2\frac{A_0 A_2}{r|\mathbf{r}-\mathbf{r}_2|}\cos[k(r-|\mathbf{r}-\mathbf{r}_2|)]\right\}.\end{aligned} \tag{4}$$

The first two terms account for scattering from isolated objects and are smoothly varying backgrounds. The third term represents classical interference from the two objects, whereas the terms in curly brackets are due to interference between the source and each object and represent holographic interference. Note that for holography to work, amplitudes A_1 and A_2 of the scattered waves must be much smaller than that of the reference wave, making the classical interference term, quadratic in the scattered waves, negligible. Because the vectors $|\mathbf{r} - \mathbf{r}_1|$ and $|\mathbf{r} - \mathbf{r}_2|$ are of comparable length in a typical DIHM setup, the spatial frequency of the classical interference pattern will be much smaller than that of the contribution from the holographic terms. Thus recording the fine spatial details of a hologram is a prerequisite to high-resolution reconstruction. Obtaining optimal sampling in the hologram thus demands proper positioning of the recording screen from the source for a given pixel size. Also note that for small objects their scattering amplitude is small compared with the amplitude of the reference wave, $A_1, A_2 \ll A_0$, ensuring that the holographic terms will be more prominent in the hologram by amplitude as well. Finally, a trivial point: The wavelength itself of course controls the spatial frequencies of our interferogram, so that it will be an important factor in establishing the maximal resolution obtainable in DIHM or in any other type of microscopy.

2. Lateral Resolution

In this section we first derive a criterion for lateral resolution in terms of the geometric parameters of DIHM; this criterion is then demonstrated with numerical simulations. For simplicity, we assume that the experimental setup has the recording screen perpendicular to the optical axis that connects the source with the center of the screen. The object consists of two point sources positioned symmetrically from the optical axis and on a line parallel to the screen so that $|\mathbf{r}_1| = |\mathbf{r}_2|$. Then the holographic term in Eq. (4) can be rewritten as

$$\tilde{I}(\mathbf{r}) = 4\frac{A_0 A_1}{r|\mathbf{r}-\mathbf{r}_1|}\cos[k(2r - |\mathbf{r}-\mathbf{r}_1| - |\mathbf{r}-\mathbf{r}_2|)/2] \times \cos[k(|\mathbf{r}-\mathbf{r}_1| - |\mathbf{r}-\mathbf{r}_2|)/2]. \tag{5}$$

The second cosine term produces the modulation of the holographic interference pattern and has maxima when its argument is $2\pi n$. To recover the necessary information from this term, we must ensure that at least the zero-order and first-order maxima are recorded on the screen. Hence it follows that two points can be resolved laterally if their lateral separation satisfies

$$|\mathbf{r}_2 - \mathbf{r}_1| \geq \frac{\lambda}{2\mathrm{NA}}, \tag{6}$$

where the numerical aperture of the microscope is

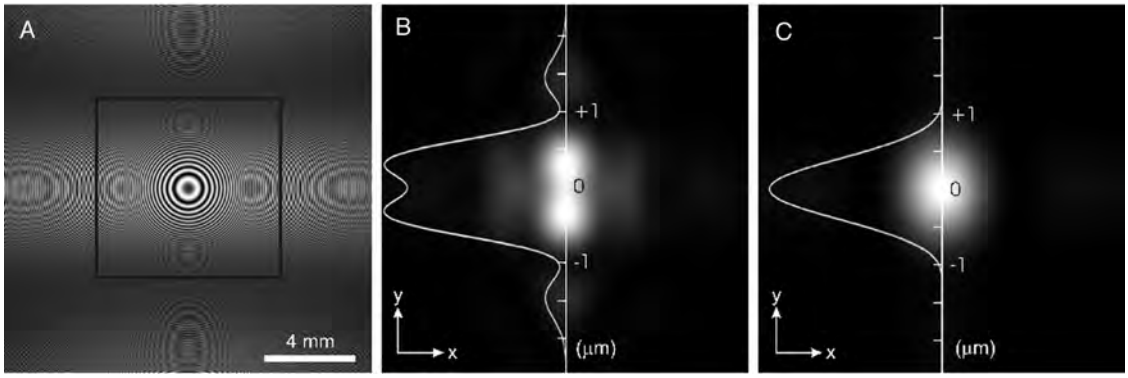

Fig. 2. Test of lateral resolution. A, Simulated hologram of two points close to the optical axis and 0.8 μm apart, taken with a blue laser with λ = 4730 Å and a numerical aperture of 0.5 (0.28 for the inner square). B, Reconstruction from the full hologram, with the intensity profile showing submicrometer resolution. C, Same as B but for the smaller hologram, showing a loss of resolution.

given by NA = sin $\theta_m = (W/2)[(W/2)^2 + D^2]^{1/2}$ with W being the screen width and D the distance form the point source to the screen. Not surprisingly, this is the same criterion as that of classical optics, although its origin is quite different. To be more specific to holography, we recall from early research on electron holography[26] that the Kirchhoff–Helmholtz transform, yielding the reconstructed amplitude, can be obtained analytically and reads, when restricted to s-wave scattering as appropriate for electromagnetic radiation, as follows:

$$K(\mathbf{r}) = A\sum_i \sum_{n=0}^{\infty} (-1)^{n/2} a_n P_n\left(\frac{z - z_i}{|\mathbf{r} - \mathbf{r}_i|}\right) j_n(k|\mathbf{r} - \mathbf{r}_i|). \tag{7}$$

The point objects (atoms in the case of electron holography) are located at positions $\mathbf{r}_i$; P_n and j_n are Legendre polynomials and spherical Bessel functions, respectively. The coefficient A is proportional to the scattering probability, and

$$a_n = (n + 1/2)\int_{\cos\theta_m}^{1} P_n(t)\mathrm{d}t \tag{8}$$

accounts for the numerical aperture, $\cos^2\theta_m = 1 - (\mathrm{NA})^2$. Recall that only the spherical Bessel function of the zero order has a maximum at the zero argument so that only the $n = 0$ term peaks at the original positions of the objects. With the intensity of the reconstructed image given by $I = |K(\mathbf{r})|^2$, we set its first and second derivatives with respect to the line connecting two point objects (this is easy in the above geometry) equal to zero to establish the modified Sparrow criterion for resolution.

As an example, we show in Fig. 2A a simulated hologram of two points separated by 0.8 μm taken with blue light and a numerical aperture of 0.5. This should, in reconstruction, yield a clear separation of the two objects, as is indeed seen in Fig. 2B. Note that the points themselves are smeared out and that their shape is controlled by the square of a spherical Bessel function of zero order, i.e., $[\sin(k\rho)/\rho]^2$, where ρ is the radial distance from the center of a point. If we reduce the numerical aperture by taking only the inner square of Fig. 2A with half the length of its sides, the numerical aperture is reduced to 0.28, and micrometer resolution is no longer achievable, as confirmed in Fig. 2C.

3. Depth Resolution

We next address the issue of depth resolution. Similar to the discussion of lateral resolution, here we find that two points can be resolved in depth if

$$|\mathbf{r}_2 - \mathbf{r}_1| \geq \frac{\lambda}{2(\mathrm{NA})^2}. \tag{9}$$

Clearly, depth resolution in holographic reconstruction is harder to achieve, and only when the hologram is recorded on a large screen can optimal resolution be achieved both laterally and in depth. We illustrate this point in Fig. 3. The problem of poor depth resolution was also encountered in photoelectron and low-energy electron diffraction (LEED) holography, and a remedy was suggested and successfully implemented by using the superposition of reconstructed images for several wavelengths.[48,55]

4. Pinhole Size

For the pinhole to act as a point source for a coherent spherical wave, its size must be of the order of a wavelength. A larger pinhole has two effects: (1) It leads to a reduction of the spatial coherence, and (2) it narrows the zero-order emission cone used to form the holographic interference pattern of emitted light. When the pinhole is illuminated with a laser, it is actually the second effect that affects the quality of holograms more. We can obtain the numerical aperture of the emission cone of a pinhole by numerically evaluating the Fresnel integral for a circular pinhole of diameter d_p. Here 84% of the diffracted light is contained within the zero-order diffraction maximum, i.e., within a half-angle θ_p to the first zero.

For $d_p = \lambda$ and 4λ the numerical aperture of the emission cone is 0.77 and 0.29, respectively. Ideally

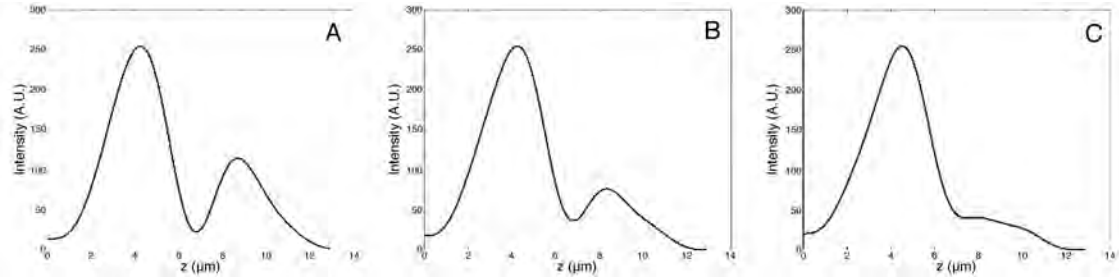

Fig. 3. Depth resolution: two point particles placed along the optical axis, 380 μm from the point source. Numerical aperture of the screen is 0.5 (512 × 512 pixels). Cuts along the optical axis for a particle separation of A, 4 μm; B, 3.5 μm; and C, 3 μm.

one would like to have this angle be larger than that formed by the recording screen; i.e., for the numerical aperture, one should minimize the decline of the intensity of the reference wave over the sample volume.

To demonstrate the effect of the pinhole size on reconstruction, we show reconstructed images of a positive USAF 1951 test target for pinholes with diameters of 2 and 0.5 μm. With the smaller pinhole, about twice the area of the test target is illuminated (compare panels A and B with D and E in Fig. 4). Whereas, not surprisingly, with the smaller pinhole, the smallest structures (228 lp/mm) are clearly resolved (see Fig. 4C); this is not the case with the larger pinhole (Fig. 4F).

5. Depth of Field

One of the most amazing advantages of holographic microscopy, and in particular of DIHM, is the fact that a single 2-D hologram produces in reconstruction a 3-D image of the object without loss of resolution. This is in sharp contrast to compound microscopy in which the depth of field reduces sharply with improved resolution, necessitating refocusing to map out a larger volume. To show this advantage, we embedded 1 μm latex beads in gelatine on a cover slide (to immobilize them), took one hologram, and made five reconstructions at different depths ranging from 300 μm to 3 mm from the cover slide (see Fig. 5). Panel A shows the hologram, and panels B and C the reconstructions at 3 and 2 mm,

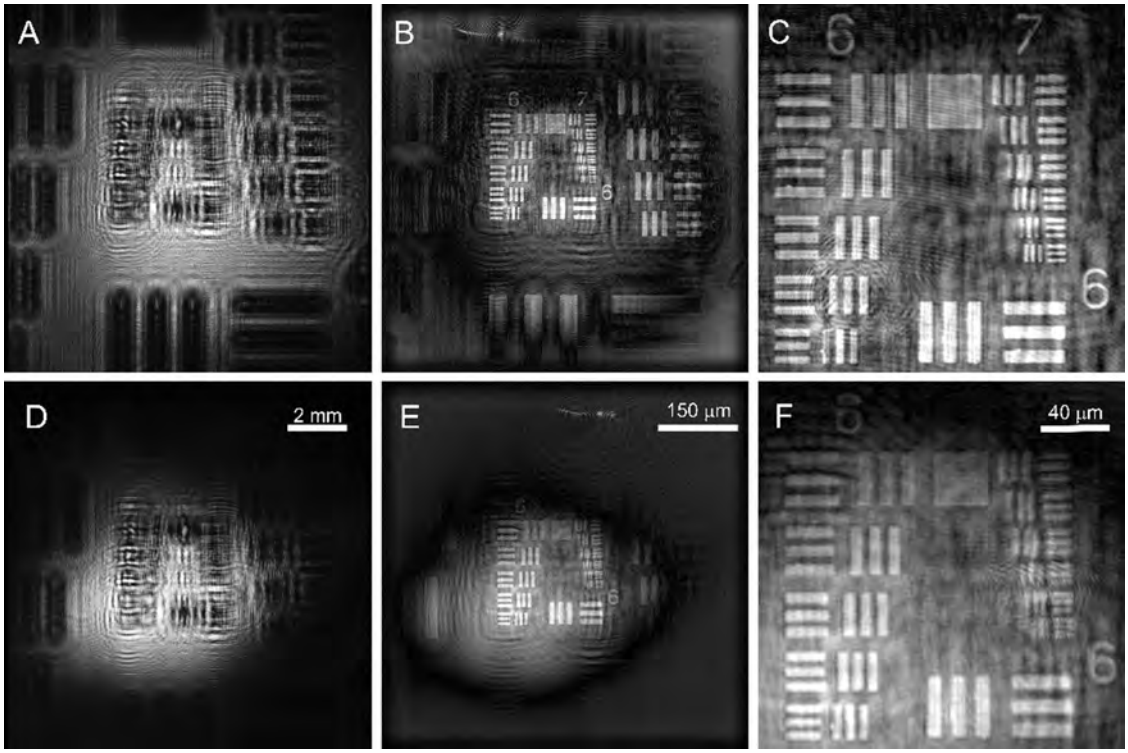

Fig. 4. Pinhole size effect: A, Hologram of a positive USAF 1951 test target taken with a 0.5 μm pinhole; B, reconstruction (after background subtraction); C, central section (groups 6 and 7) only; D–F, same but for a 2 μm pinhole. Laser wavelength of 408 nm and numerical aperture of NA = 0.208.

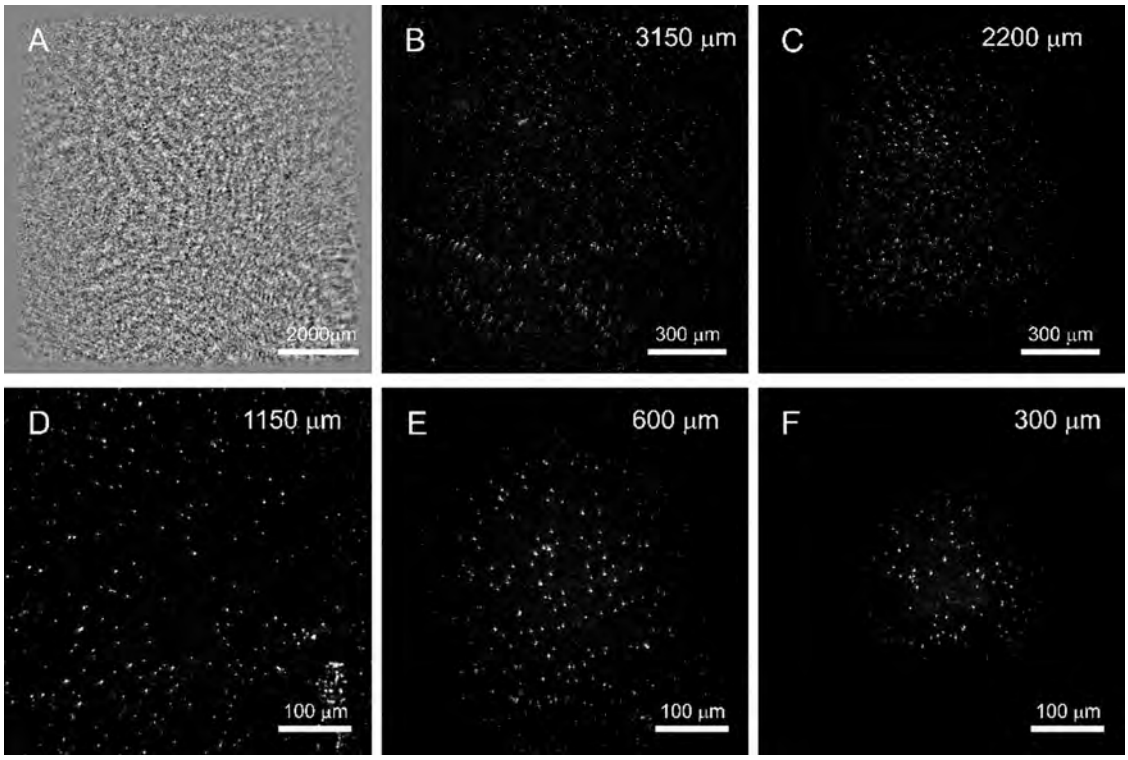

Fig. 5. Depth of field shown with 1 μm latex beads in a 150 μm thick gelatine layer on a cover slide (to immobilize them): A, Hologram and B–F, five reconstructions at different depths, ranging from 3 mm to 30 μm, from the cover slide. Pinhole diameter, 0.5 μm; numerical aperture, 0.2; $\lambda = 532$ nm.

respectively, with a field of view of 1.4 mm. In all panels, the pinhole was 0.5 μm in diameter and the numerical aperture was 0.2. The effect of the pinhole size is again seen clearly in that moving the reconstruction plane closer to the pinhole will eventually capture the outline of the finite emission cone for the same numerical aperture.

D. Twin Image Revisited

A frequently voiced criticism of DIHM, propagated in most textbooks and still repeated in the literature to this date, is connected with the so-called twin-image problem. We recall that, due to its phase sensitivity, reconstruction does not only give a structured wave amplitude at the position of the object d (the distance from the source to the object) but also at $-d$ (i.e., the same distance on the other side of the source). If, as in photoelectron holography, the source–object distance is of atomic dimensions and of the same order as the expected resolution of the method, the signal from the twin image at the location of the object is substantial, causing severe distortions of the reconstructed image. Thus ingenious methods have been devised to eliminate the twin image.[30–33,55–62] For DIHM, on the other hand, the twin image does not represent a problem. The reason is one of geometry and much akin to a similar solution to the twin-image problem achieved in Fraunhofer holography.[56] If the source–object distance is, as a typical example, several thousand times the wavelength, then the twin

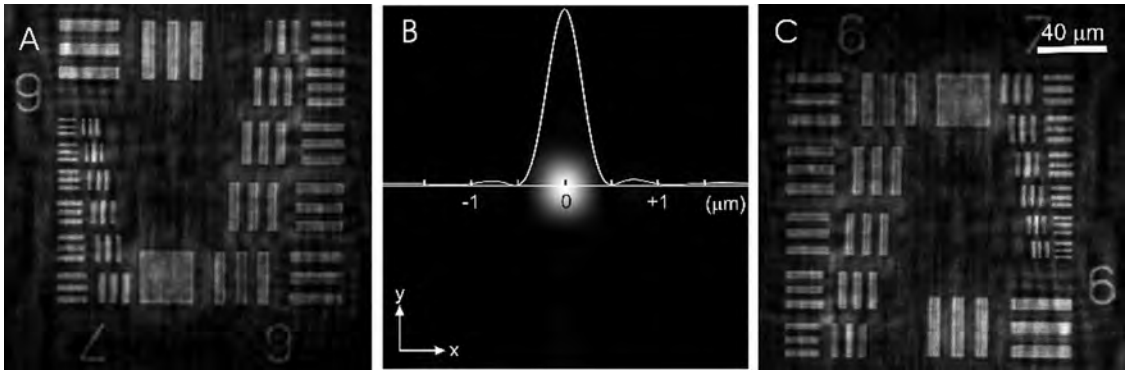

Fig. 6. A, Twin image of C (i.e., reconstructed at the same distance on the other side of the pinhole); B, reconstruction at the origin, showing the pinhole of size 0.5 μm.

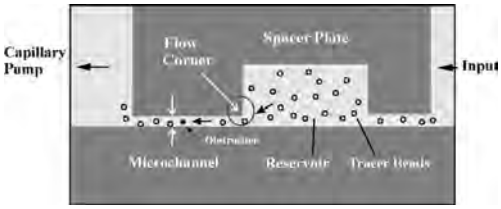

Fig. 7. Schematic diagram of the sample chamber used to study the fluid flow around obstructions. The chamber was constructed with microscope and coverslip slides. Light propagated perpendicular to the plane of the paper. The particle suspension (5 and 10 μm latex spheres in water) entered from the right and was moved through the chamber with the help of a capillary pump on the left. The microchannel contained the obstruction and the channel cross sections could be adjusted by varying the thickness of the spacer plate. The circle identifies the location of the corner flow examined.

image is the same distance on the other side of the source and the signal produced by it at the object is smeared out over the length scale of the achievable resolution for a given screen size. Thus, if one works with a large-enough numerical aperture by recording on a large screen to achieve a resolution of the order of a wavelength, the background signal introduced by the twin image is negligibly small, as we have shown before and do again here. Reducing the screen size will then not only reduce the resolution but will concurrently enhance the background signal, leading to artificial structures in the reconstructed image that may be interpreted as the twin image. Likewise, reducing the pixel density will also lead to a deterioration of the reconstructed image. To check this, we took a hologram of the test target (panel A of Fig. 4) with a high-resolution digital camera with 2048 $\times$ 2048 pixels, from which reconstructed images were obtained. We then eliminated every second pixel (in each direction), resulting in a digital image of 1024 $\times$ 1024 pixels; this does not lead to deterioration yet. However, a further reduction will lead to a violation of the Nyquist theorem, i.e., keeping fewer than 2 pixels for the smallest fringe, and thus to a noticeable degradation of the resolution and an enhancement of the noise background.

We hasten to add that the same deterioration will take place if uncontrolled approximations are made in reconstruction Eq. (2), such as an on-axis approximation discussed above. To summarize, the twin image is not a problem in DIHM in that it can be reduced below the noise level by using a large-enough recording screen (for an object of a given size) such that, in principle, one achieves the desired resolution (of the order of a wavelength). At the same time, it is mandatory that one uses the Kirchhoff–Helmholtz reconstruction formalism without approximations.

To demonstrate the absence of the twin-image problem in DIHM, we show in Fig. 6C a reconstruction of the inner part of the USAF 1951 test target as in Fig. 4C, with the difference being that the hologram underlying this reconstruction was taken with a numerical aperture of 0.5. The resolution is not better because the smallest structures, group 7, are 4 μm apart, which is easily resolved according to relation (6) by a numerical aperture of 0.2. In panel A we show the twin image; i.e., a reconstruction at the same distance from the pinhole as the real image in panel C but on the other side of the pinhole. These images are obviously inverted copies of each other and do not interfere with each other. Further proof of the absence of twin-image noise can be found in the experimental results that we present below and also in previous studies published by us.

We can also use the reconstruction algorithm to measure the pinhole itself by performing the reconstruction in a plane through the origin. The result is shown in Fig. 6B. The half-width of the intensity peak is 0.5 μm or λ. Needless to say, nothing like this could be accomplished with the on-axis approximation.

3. Digital In-Line Holographic Microscopy Examples

To demonstrate the state of the art in DIHM, we now show a number of applications in microfluidics, biology, and underwater DIHM.

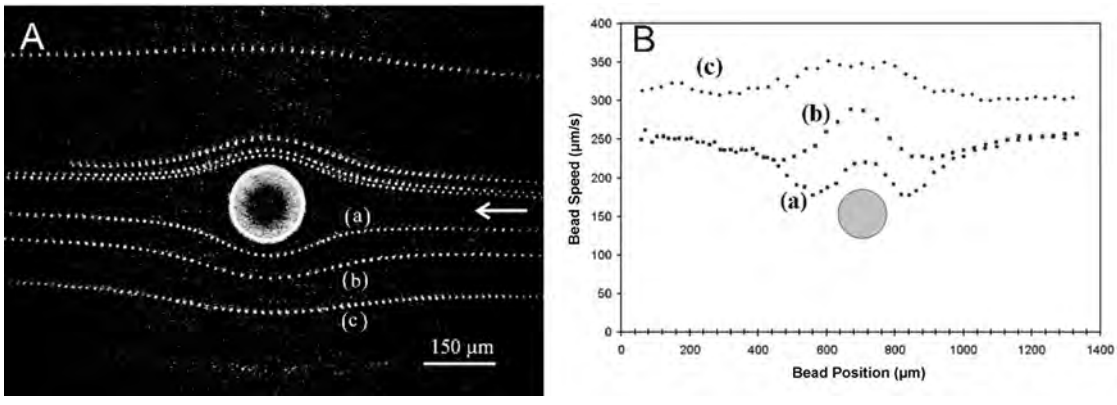

Fig. 8. Flow of 5 μm tracer beads around a 140 μm sphere. A, Reconstruction from a difference hologram of 200 individual holograms taken 67 ms apart in the equatorial plane of the sphere. Arrow indicates flow direction. (λ = 532 nm, NA = 0.2). B, Local fluid speed calculated from successive positions along traces (a), (b), and (c) in A. Results for trace (c) were displaced upward by 100 μm/s for clarity.

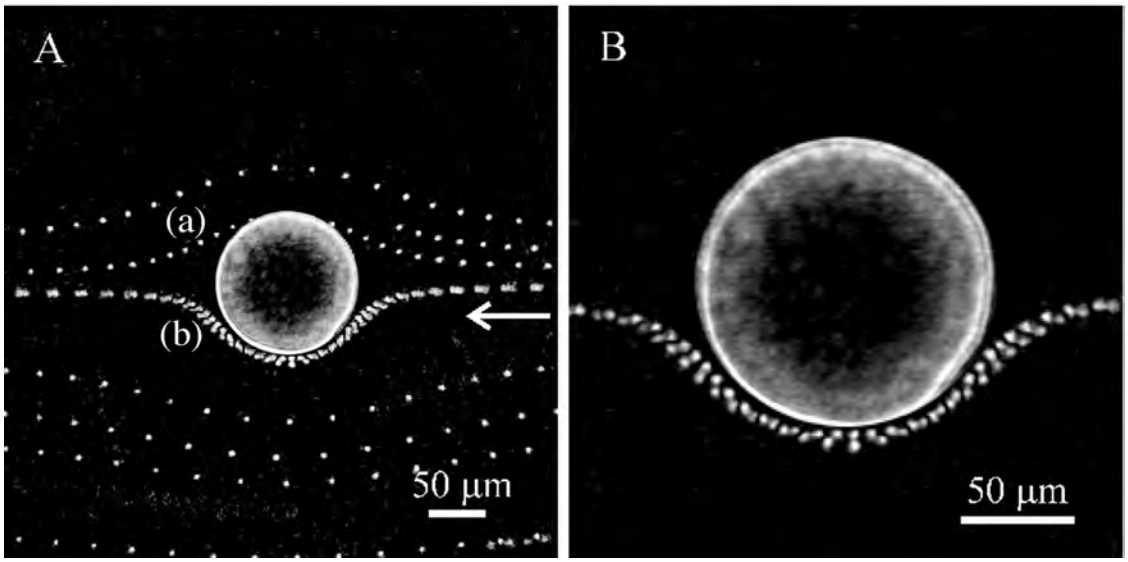

Fig. 9. Stream lines around a stationary sphere reconstructed from a difference hologram. A, Stream line (a) was 24 μm above that of stream line (b) and is partially obscured by the sphere. Stream line (b) shows the trajectory of a bead dimer and illustrates the action of shear forces near the bead boundary that cause the dimer to tumble. B, Enlarged view of the dimer trajectory.

A. Microfluidics

Understanding the flow of fluids through micrometer-sized channels is of great importance in many areas of science and engineering. The flow may be influenced by complex boundary effects, it may not follow simple Newtonian rules, or it may be influenced by suspended particles such that numerical modeling of the flow becomes difficult or impossible.

Modern micromachining methods have allowed the construction of microfluidic devices that have had a particularly significant effect on the development of novel biomedical instrumentation. Some of these involve the motion of macromolecules, vesicles, or even whole cells through narrow channels, and the flow can also be accompanied by biochemical processes between suspended components or with the channel walls. Other device applications involve the separation of cells in fluid channels with the help of electrophoretic or dielectrophoretic forces.[63–65] Other microelectromechanical systems (MEMS) devices have been developed to facilitate the mixing of two fluids on a microfluid scale. Since microfluid flow is generally a low-Reynolds-number flow, vortex mixing in microchannels does not occur and it is important to capture experimentally the effectiveness of methods that may be devised to produce mixing. Another important microfluidics area is the study of fluid flow induced by the locomotion of micro-organisms such as algae and various plankton species. This is a particularly challenging field since it is difficult with standard microscopic methods to simultaneously follow the motion of the organism as well as that of tracer particles that may be in its vicinity but are sufficiently removed to be out of focus. We describe here an application of DIHM that can capture fluid flow with a depth of field not achievable with conventional optical microscopy.

To record the stream lines for fluid moving around obstructions, the fluid was seeded with 5 or 10 μm diameter latex beads, and several hundred holograms of the fluid motion were recorded over a period of several minutes. Difference holograms were then constructed, and these were summed to give the final hologram data set. If holograms are collected over an extended time period, then hologram summation implies that mapping of the flow field can be performed with a low concentration of tracer beads.

For the observation of flow around obstructions, we used flow chambers constructed with microscope

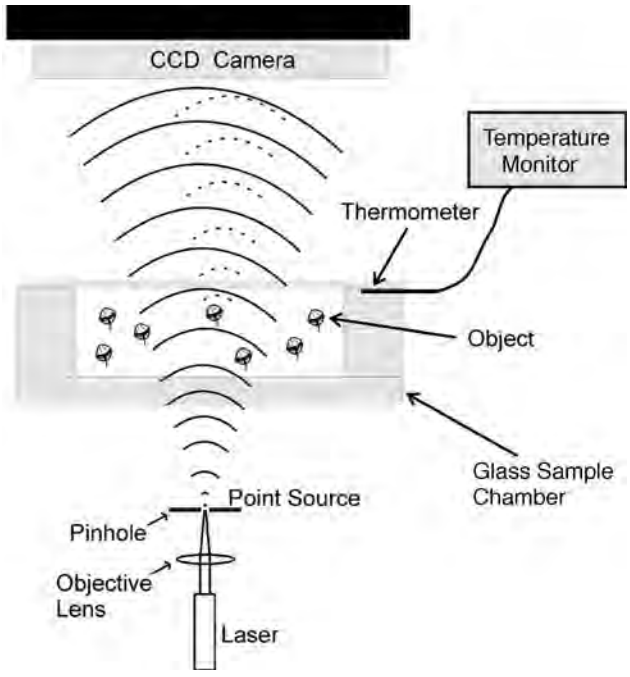

Fig. 10. Experimental arrangement for biological applications.

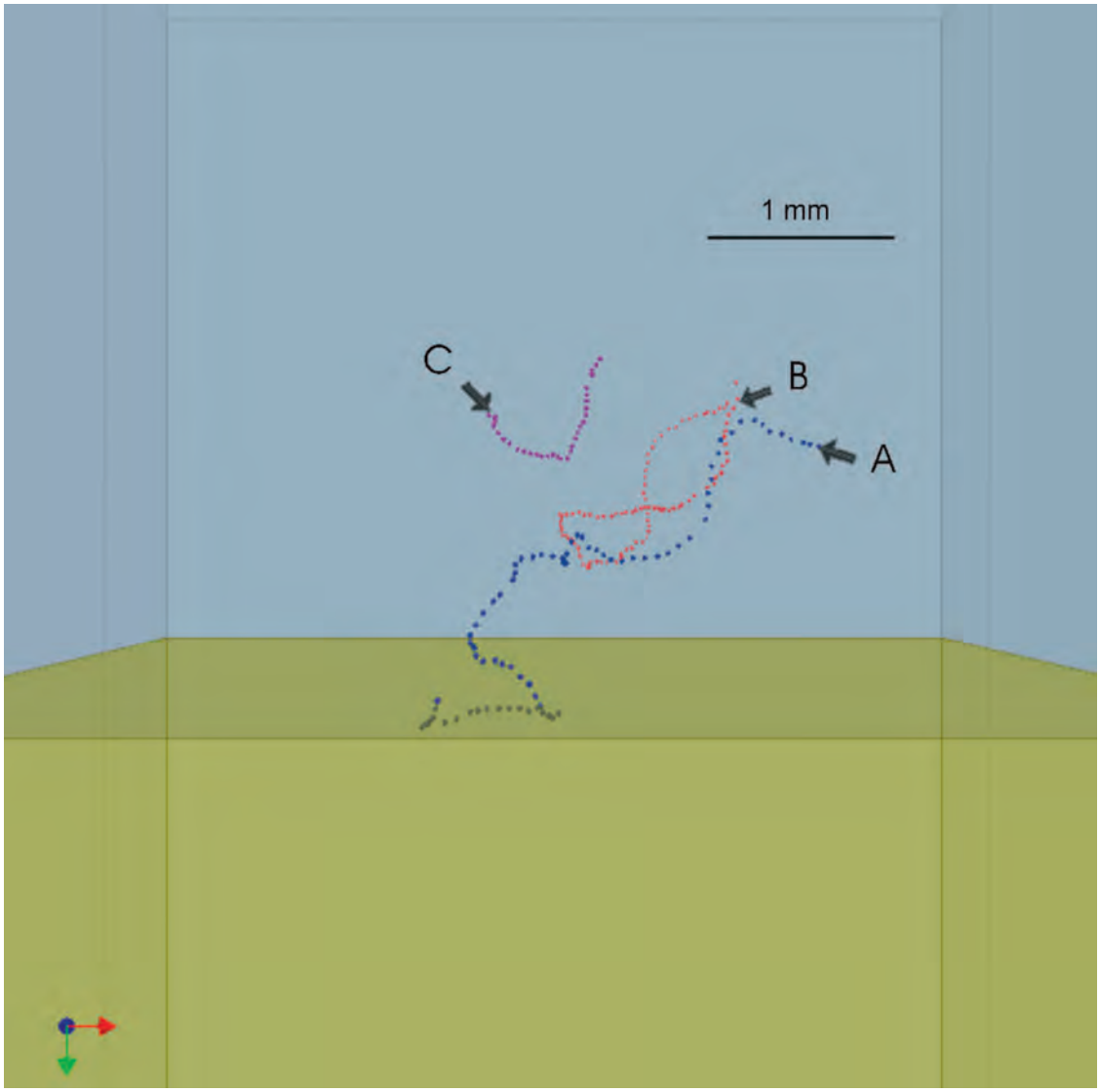

Fig. 11. (Color online) Three-dimensional rendering of the motion of algae in seawater approaching a concentrated salt solution in the lower half of the tank.

slides and coverslips as shown in Fig. 7. The particle suspension was added on the right and was moved through the channel through a capillary pump on the left. For the observation of flow past a spherically shaped obstruction, single metal spheres were attached to the bottom center of the flow channel. The spheres ranged in diameter from 80 to 150 μm. The channel size for these experiments was 2 mm in width and 0.3 mm in depth. Observations of fluid motion induced by a moving sphere were performed in a drop chamber with a cross section of 15 mm × 1 mm and a height of 20 mm. Spheres were placed near the center of the chamber opening before release.

The experiments were performed with either green ($\lambda = 532$ nm) or blue ($\lambda = 473$ nm) laser light, and the holograms were recorded with a CCD camera (Megaplus Es 1.0/MV; 1008 × 1018 pixels; pixel size of 9 μm × 9 μm). The camera could record images at 15 frames/s with a minimum shutter speed of 0.8 ms. All experiments were performed with a 1 μm diameter pinhole. The position resolution in DIHM of latex particles was investigated in detail previously by Xu *et al.*[38] Under favourable conditions, the coordinates of beads could be determined to ±50 nm. In most of our studies the data-acquisition time was of the order of a few seconds and diffusion distances of the tracer beads were much less than the bead diameters and could be neglected. All hologram reconstructions were performed in planes that were perpendicular to the line joining the pinhole with the center of the CCD chip.

Consider an example of a difference hologram (from 200 individual holograms) for fluid flowing around a 140 μm diameter metal sphere attached to the bottom of a 300 μm deep channel. A reconstruction of this hologram in a lateral plane that passes through the center of the metal sphere is displayed in Fig. 8A. The expected laminar flow around the sphere is clearly visible. The tracer particles in some of the

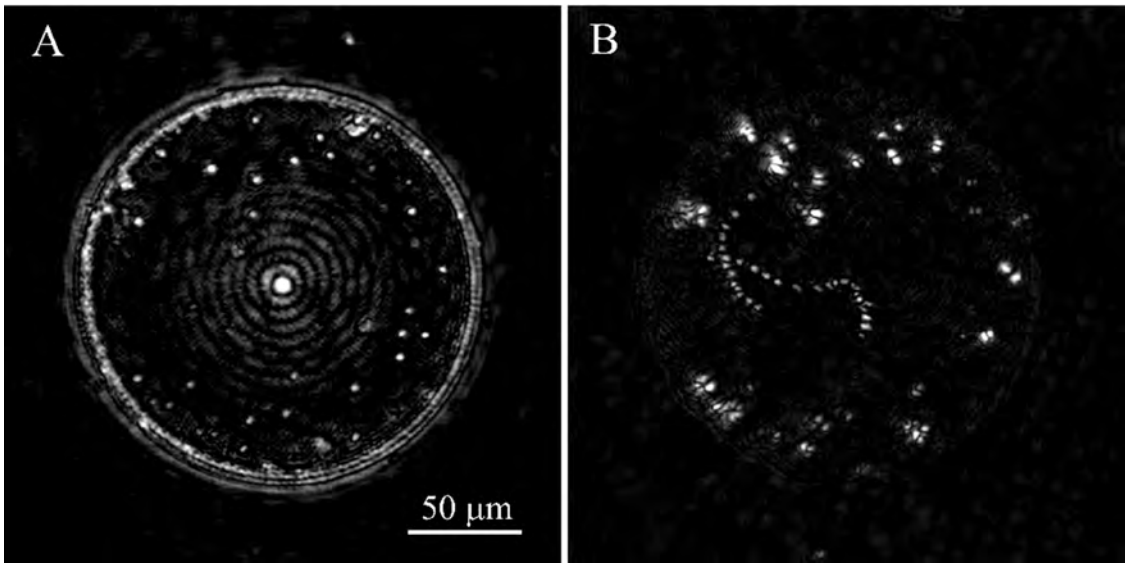

Fig. 12. Bacteria in a diatom (*Coscinodiscus wailesii*). A, Reconstruction from one hologram showing the siliceous outer shell with labiate processes (bright spots); B, reconstruction of bacterial trajectories from a difference hologram composed of a time series of 20 holograms taken 1.3 s apart. Green laser; 0.5 μm pinhole; pinhole to sample (diatom), 1 mm; numerical aperture, 0.22.

stream lines in Fig. 8A appear somewhat blurred because the corresponding stream lines lie outside the particular reconstruction plane chosen. By adjusting the reconstruction depth appropriately, these out-of-focus particles can be brought into focus, and their Z position in the fluid channel can be determined. In this way flow information about the whole fluid volume can be extracted. The vector connecting two subsequent positions of a particle along its stream line gives its local velocity. We can also determine the spatial coordinates of the tracer bead along its stream line and from these calculate the local speed of the fluid. The speed variations along three stream lines in Fig. 8A are shown in Fig. 8B.

The fact that the fluid velocity has not assumed a constant value at a distance of 700 μm upstream and downstream from the sphere is a manifestation of the long-range effect of the sphere in Stokes flow. The velocity gradient near the surface of the metal sphere is particularly well captured by the movement of a bead dimer in Fig. 9. Far away from the metal sphere, the dimer axis is parallel to the stream line. As the dimer approaches the sphere, fluid shear causes the dimer to tumble. It aligns itself again with the stream line after leaving the sphere behind.

B. Biology

For applications of DIHM in biology, we used the experimental arrangement shown in Fig. 10. It has been used to study the swimming behavior of algae *Alexandrium* as a function of temperature, demonstrating, for instance, that at elevated temperatures (21 °C) their normal behavior to swim in more or less straight lines changes dramatically to exclusively circular motion owing to the loss of posterior flagellae.[44] Here we present results regarding the effect of increased salinity. To this effect, we used a pipette to introduce saturated salt water below a layer of seawater. Figure 11 shows a 3-D rendering of the trajectories of algae obtained from a stack of 50 reconstructions. Trajectory A was taken immediately after the saltwater was introduced, implying a sharp interface. The alga does not sense any danger until it crosses the interface and gets poisoned. Half an hour later the saltwater has diffused upward and the alga (B) are warned and turn around. Another half-hour later, warning occurs even farther away from the interface at trajectory C.

We next look at a diatom in seawater, species *Coscinodiscus wailesii*. It is a round single-cell plant, typically 230–370 μm in diameter, and is abundant in plankton, particularly in warmer oceans. In Fig. 12A we show a reconstruction from a single hologram, showing clearly the siliceous outer shell and a number of labiate processes that appear as bright dots. We also took a movie of 20 holograms with the frames taken 1.3 s apart, from which we constructed a difference hologram by adding and subtracting. Because the diatom did not move much as a whole over the time span of 26 s, the outer shell does not show up in the reconstruction. Some of the labiate processes did move and show up as closely spaced dots in the reconstruction (see Fig. 12B). Because the construction of the difference holograms removes not only information about stationary structures such as dirt but also artifacts due to imperfection in the laser, weaker structures are more pronounced. In our case it is the motion of bacteria inside the diatom; see the two tracks of tiny dots in Fig. 12B. These bacteria are less than 1.5 μm in diameter, and their speed is between 3.5 and 8 μm/s.

This example clearly shows that the construction of the difference hologram to capture motion leads automatically to higher resolution in the sense that less

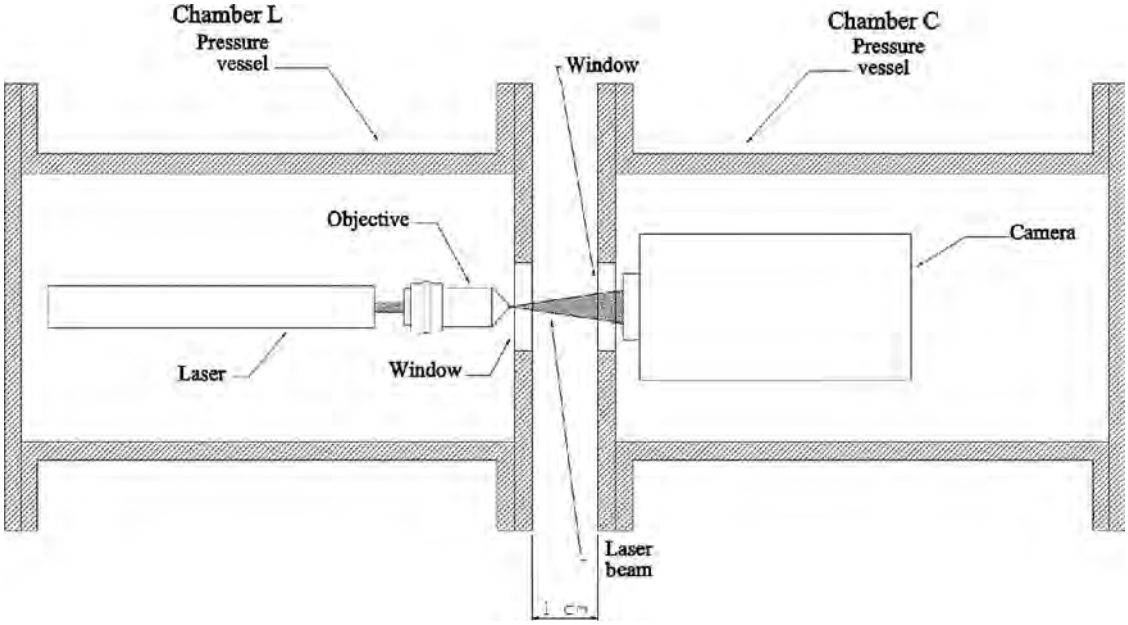

Fig. 13. Underwater DIHM.

prominent features, i.e., much smaller and thus weaker scatterers, can be made visible. One can hope that with this procedure microscopic processes, such as the attachment of algae to cell walls or nuclei and cell division, can be studied as well. Again, the capability of the scalable convolution algorithm for reconstruction[19] is crucial to this procedure's success.

C. Underwater Digital In-Line Holographic Microscopy

To allow for observations with DIHM in ocean or lake environments, we constructed an underwater microscope. Its schematic is shown in Fig. 13. The microscope consists of two pressure chambers, one of which contains the laser and the other the CCD camera (plus power supply). The two chambers are kept at a fixed distance from each other to allow water to freely circulate between them. In the center of the chamber plates facing each other are small windows, with the one on the laser chamber having the pinhole. The signal from the CCD camera is transmitted via an underwater USB cable to a buoy or a boat above, from where a satellite link can be established for data transmission to a laboratory. Depending on the design of the pressure chamber, water depths of several hundred meters should easily be possible; our prototype has operated at a 15 m depth and has given the same performance as far as resolution is concerned as the desktop version of DIHM.

In Fig. 14 we show a few species swimming through the observation channel of the underwater DIHM. In panel A we show the reconstructed image of *Paramecium* (length, 320 μm; width, 46.8 μm). Panels

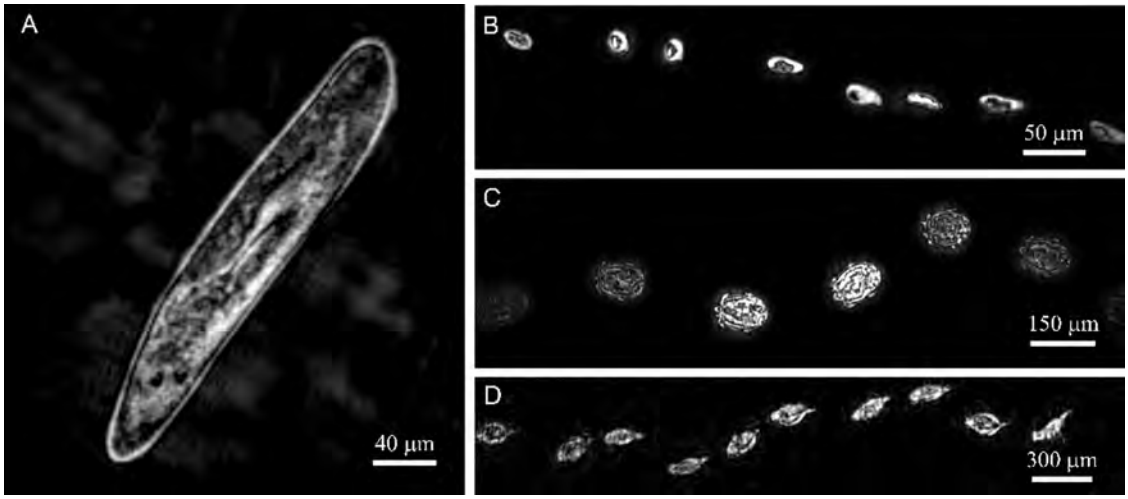

Fig. 14. Images taken with the underwater DIHM. A, *Paramecium* (length, 320 μm; width, 46.8 μm). B–D, Trajectories of various species swimming through the observation window, with a frame rate of 10 frames/s. B, *Ciliate* (length, 25 μm; width, 13 μm); C, *Didinium* (length, 133 μm; width, 77 μm); D, *Rotifer* (length, 200 μm; width, 100 μm).

B–D show the trajectories of various species, reconstructed from a difference hologram of holograms taken at a rate of 10 frames/s. In panel B we show the trajectory of a *Ciliate* (length, 25 μm; width, 13 μm) swimming at a speed of 450 μm/s. Panel C shows a *Didinium* (length, 133 μm; width, 77 μm) swimming at a speed of 2.1 μm/s. Panel D shows a *Rotifer* (length, 200 μm; width, 100 μm) swimming at a speed of 2.5 μm/s.

4. Summary and Outlook

We want to conclude by underlining some remarkable characteristics of DIHM and the underwater DIHM:

1. Simplicity of the microscope: DIHM, as well as underwater DIHM, is microscopy without objective lenses. The hardware required for the desktop version is a laser, a pinhole, and a CCD camera. For the underwater DIHM version, we need the same elements contained in a submersible hermetic shell.
2. Maximum information: A single hologram contains all the information about the 3-D structure of the object. A set of multiple holograms can be properly added to provide information about 4-D trajectories of samples.
3. Maximum resolution: Optimal resolution, of the order of a wavelength of the laser, can be obtained easily with both versions.
4. Simplicity of sample preparation: This is particularly true for biological samples in which no sectioning or staining are required, so that living cells and specimens can be viewed. Indeed, for the underwater DIHM, there is no sample preparation at all, and real-time information of living organisms can be retrieved.
5. Speed: The kinetics of the sample, such as particle motion or metabolic changes in a biological specimen, can ultimately be followed at the capture rate of the image-acquisition system.
6. Four-dimensional tracking: A large number of particles can be tracked simultaneously in 3-D as a function of time.

Regarding 4-D tracking, which is feasible in both versions of the DIHM, we emphasize the efficiency in data collection in our procedure. Removal of background effects and construction of summed holograms are easily accomplished so that high-resolution tracking of many particles in 4-D can be obtained from just one difference hologram. Since resolutions of the order of a wavelength of light have been achieved with DIHM, tracking of organisms as small as bacteria is possible, as would be the motion of plankton in water or, at lower resolution, the aerial trajectories of flying insects. DIHM can also be used successfully on macroscopic biological specimens, prepared by standard histological procedures, as for a histological section of the head of the fruit fly, *Drosophila melanogaster*. Such images reveal the structure of the pigmented compound eye and different neuropile regions of the brain within the head cuticle, including the optic neuropiles underlying the compound eye.[39]

Outside biology, applications of 4-D DIHM have been demonstrated in microfluidics for particle velocimetry, i.e., tracking of the motion of particles in a liquid or gas flows, and gas evolution in electrolysis and in the visualization of structures in convective or turbulent flow. Further applications will deal with colloidal suspensions, remote sensing, environmental monitoring, investigation of bacterial attachment to surfaces and biofilm formation, and many more. DIHM, with its inherent capability of obtaining magnified images of objects (unlike conventional off-axis holography), is therefore a powerful new tool for a large range of research fields. Films on 4-D tracking and more examples can be viewed at http://www.physics.dal.ca/~kreuzer.

This research was supported through grants from the Natural Sciences and Research Council of Canada and the Office of Naval Research in Washington, D.C.

References

1. D. Gabor, "A new microscopic principle," Nature **161,** 777–778 (1948).
2. E. N. Leith and J. Upatnieks, "Reconstructed wavefronts and communication theory," J. Opt. Soc. Am. **52,** 1123–1130 (1962).
3. E. N. Leith and J. Upatnieks, "Wavefront reconstruction with continuous-tone objects," J. Opt. Soc. Am. **53,** 1377–1381 (1963).
4. E. N. Leith and J. Upatnieks, "Wavefront reconstruction with diffused illumination and three-dimensional objects," J. Opt. Soc. Am. **54,** 1295–1301.
5. P. Hariharan, *Optical Holography* (Cambridge U. Press, 1996).
6. T. Kreis, *Holographic Interferometry* (Akademie Verlag, 1996).
7. Y. Aoki, "Optical and numerical reconstruction of images from sound-wave holograms," IEEE Trans. Acoust. Speech **AU-18,** 258–267 (1970).
8. M. A. Kronrod, L. P. Yaroslavski, and N. S. Merzlyakov, "Computer synthesis of transparency holograms," Sov. Phys. Tech. Phys. **17,** 329–332 (1972).
9. T. H. Demetrakopoulos and R. Mittra, "Digital and optical reconstruction of images from suboptical diffraction patterns," Appl. Opt. **13,** 665–670 (1974).
10. L. Onural and P. D. Scott, "Digital decoding of in-line holograms," Opt. Eng. **26,** 1124–1132 (1987).
11. G. Liu and P. D. Scott, "Phase retrieval and twin-image elemination for in-line Fresnel holograms," J. Opt. Soc. Am. A **4,** 159–165 (1987).
12. L. Onural and M. T. Oezgen, "Extraction of three-dimensional object-location information directly from in-line holograms using Wigner analysis," J. Opt. Soc. Am. A **9,** 252–260 (1992).
13. H.-W. Fink, "Point source for electrons and ions," IBM J. Res. Dev. **30,** 460–463 (1986).
14. H.-W. Fink, "Point source for electrons and ions," Phys. Scr. **38,** 260–263 (1988).
15. W. Stocker, H.-W. Fink, and R. Morin, "Low-energy electron and ion projection microscopy," Ultramicroscopy **31,** 379–384 (1989).
16. H.-W. Fink, W. Stocker, and H. Schmid, "Holography with low-energy electrons," Phys. Rev. Lett. **65,** 1204–1206 (1990).
17. H.-W. Fink, H. Schmid, H. J. Kreuzer, and A. Wierzbicki, "Atomic resolution in lens-less low-energy electron holography," Phys. Rev. Lett. **67,** 1543–1546 (1991).
18. H. J. Kreuzer, K. Nakamura, A. Wierzbicki, H.-W. Fink, and

H. Schmid, "Theory of the point source electron microscope," Ultramicroscopy **45,** 381–403 (1992).
19. H. J. Kreuzer and R. P. Pawlitzek, LEEPS, Version 1.2: a software package for the simulation and reconstruction of low energy electron point source images and other holograms, (Helix Science Applications, Halifax, Nova Scotia, Canada, 1993–1998).
20. S. Horch and R. Morin, "Field emission from atomic size sources," J. Appl. Phys. **74,** 3652–3657 (1993).
21. H.-W. Fink, H. Schmid, and H. J. Kreuzer, "State of the art of low-energy electron holography," in *Electron Holography,* A. Tonomura, L. F. Allard, D. C. Pozzi, D. C. Joy, and Y. A. Ono, eds. (Elsevier Science B.V., 1995).
22. H.-W. Fink, H. Schmid, E. Ermantraut, and T. Schulz, "Electron holography of individual DNA molecules," J. Opt. Soc. Am. A **14,** 2168–2172 (1997).
23. A. Gölzhäuser, B. Völkel, B. Jäger, M. Zhamikov, H. J. Kreuzer, and M. Grunze, "Holographic imaging of macromolecules," J. Vac. Sci. Technol. A **16,** 3025–3028 (1998).
24. H. Schmid, H.-W. Fink, and H. J. Kreuzer, "In-line holography using low-energy electrons and photons: applications for manipulation on a nanometer scale," J. Vac. Sci. Technol. B **13,** 2428–2431 (1995).
25. H. J. Kreuzer, H.-W. Fink, H. Schmid, and S. Bonev, "Holography of holes, with electrons and photons," J. Microsc. **178,** 191–197 (1995).
26. H. J. Kreuzer, "Low energy electron point source microscopy," Micron **26,** 503–509 (1995).
27. H. J. Kreuzer, N. Pomerleau, K. Blagrave, and M. H. Jericho, "Digital in-line holography with numerical reconstruction," in *Interferometry '99: Techniques and Technologies,* M. Kujawinska and M. Takeda, eds., Proc. SPIE **3744,** 65–74 (1999).
28. P. Marquet, B. Rappaz, P. Magistretti, E. Cuche, Y. Emery, T. Colomb, and C. Depeursinge, "Digital holographic microscopy: a noninvasive contrast imaging technique allowing quantitative visualization of living cells with subwavelength axial accuracy," Opt. Lett. **30,** 468–470 (2005).
29. M. K. Kim, "Wavelength-scanning digital interference holography for optical sectioning imaging," Opt. Lett. **24,** 1693–1695 (1999).
30. I. Yamaguchi and T. Zhang, "Phase-shifting digital holography," Opt. Lett. **22,** 1268–1270 (1997).
31. T. Zhang and I. Yamaguchi, "Three-dimensional microscopy with phase-shifting digital holography," Opt. Lett. **23,** 1221–1223 (1998).
32. I. Yamaguchi, J. Kato, S. Ohta, and J. Mizuno, "Image formation in phase-shifting digital holography and applications to microscopy," Appl. Opt. **40,** 6177–6186 (2001).
33. T.-C. Poon, "Recent progress in optical scanning holography," J. Holography Speckle **1,** 6–25 (2004).
34. T.-C. Poon, K. Doh, B. Schilling, M. Wu, K. Shinoda, and Y. Suzuki, "Three-dimensional microscopy by optical scanning holography," Opt. Eng. **34,** 1338–1344 (1995).
35. B. W. Schilling, T.-C. Poon, G. Indebetouw, B. Storrie, K. Shinoda, Y. Suzuki, and M. Wu, "Three-dimensional holographic fluorescence microscopy," Opt. Lett. **22,** 1506–1508 (1997).
36. G. Indebetouw, P. Klysubun, T. Kim, and T.-C. Poon, "Imaging properties of scanning holographic microscopy," J. Opt. Soc. Am. A **17,** 380–390 (2000).
37. J. Swoger, M. Martinez-Corral, J. Huisken, and E. Stelzer, "Optical scanning holography as a technique for high-resolution three-dimensional biological microscopy," J. Opt. Soc. Am. A **19,** 1910–1918 (2002).
38. W. Xu, M. H. Jericho, I. A. Meinertzhagen, and H. J. Kreuzer, "Digital in-line holography of microspheres," Appl. Opt. **41,** 5367–5375 (2002).
39. W. Xu, M. H. Jericho, I. A. Meinertzhagen, and H. J. Kreuzer, "Digital in-line holography for biological applications," Proc. Natl. Acad. Sci. USA **98,** 11,301–11,305 (2001).
40. H. J. Kreuzer, M. H. Jericho, I. A. Meinertzhagen, and W. Xu, "Digital in-line holography with photons and electrons," J. Phys. Condens. Matter **13,** 10,729–10,741 (2001).
41. H. J. Kreuzer, M. H. Jericho, and W. Xu, "Digital in-line holography with numerical reconstruction: three-dimensional particle tracking," in *Recent Developments in Traceable Dimensional Measurements,* J. E. Decker and N. Brown, eds., Proc. SPIE **4401,** 234–244 (2001).
42. W. Xu, M. H. Jericho, I. A. Meinertzhagen, and H. J. Kreuzer, "Tracking particles in 4-D with in-line holographic microscopy," Opt. Lett. **28,** 164–166 (2003).
43. H. J. Kreuzer, M. H. Jericho, I. A. Meinertzhagen, and W. Xu, "Digital in-line holography with numerical reconstruction: 4D tracking of microstructures and organisms," in Proc. SPIE **5005,** 299–306 (2003).
44. N. I. Lewis, A. D. Cemballa, W. Xu, M. H. Jericho, and H. J. Kreuzer, "Effect of temperature in motility of three species of the marine dinoflagellate *Alexandrium*," in *Proceedings of the Eighth Canadian Workshop on Harmful Marine Algae,* S. S. Bates, ed., Can. Tech. Rep. Fish. Aquat. Sci. **2498,** 80–87 (2003).
45. W. Xu, M. H. Jericho, and H. J. Kreuzer, "Digital in-line holographic microscopy," Optik (to be published).
46. D. Gabor, "Microscopy by reconstructed wavefronts," Proc. R. Soc. London Ser. A **197,** 454–487 (1949).
47. J. J. Barton, "Photoelectron holography," Phys. Rev. Lett. **61,** 1356–1359 (1988).
48. K. Heinz, U. Starke, and J. Bernardt, "Surface holography with LEED electrons," Prog. Surf. Sci. **64,** 163–178 (2000).
49. U. Schnars and W. Jüptner, "Digital recording and numerical reconstruction of holograms," Meas. Sci. Technol. **13,** R85–R101 (2002).
50. L. P. Yaroslavskii and N. S. Merzlyakov, *Methods of Digital Holography* (translated from Russian by D. Parsons, Consultants Bureau, New York, 1989).
51. L. P. Yaroslavsky, *Digital Holography and Digital Image Processing: Principles, Methods, Algorithms* (Kluwer, 2003).
52. L. Rayleigh, *Collected Papers* (Cambridge U. Press, 1902), pp. 3, 84.
53. M. Born and E. Wolf, *Principles of Optics,* 6th ed. (Pergamon, 1993).
54. T. Asakura, "Resolution of two unequally bright points with partially coherent light," Nouv. Rev. Opt. **5,** 169–177 (1974).
55. J. J. Barton, "Removing multiple scattering and twin images from holographic images," Phys. Rev. Lett. **67,** 3106–3109 (1991).
56. J. B. DeVelis, G. Parrent, and B. J. Thompson, "Image reconstruction with Fraunhofer holograms," J. Opt. Soc. Am. **56,** 423–1427 (1996).
57. K. Doh, T.-C. Poon, and G. Indebetouw, "Twin-image noise in optical scanning holography," Opt. Eng. **35,** 1550–1555 (1996).
58. P. Sun and J.-H. Xie, "Method for reduction of background artifacts of images in scanning holography with a Fresnel-zone-plate coded aperture," Appl. Opt. **43,** 4214–4218 (2004).
59. S.-G. Kim, B. Lee, and E.-S. Kim, "Removal of bias and the conjugate image in incoherent on-axis triangular holography and real-time reconstruction of the complex hologram," Appl. Opt. **36,** 4784–4791 (1997).
60. T.-C. Poon, T. Kim, G. Indebetouw, M. H. Wu, K. Shinoda, and Y. Suzuki, "Twin-image elimination experiments for three-dimensional images in optical scanning holography," Opt. Lett. **25,** 215–217 (2000).
61. Y. Takaki, H. Kawai, and H. Ohzu, "Hybrid holographic microscopy free of conjugate and zero-order images," Appl. Opt. **38,** 4990–4996 (1999).
62. P. Korecki, G. Materlik, and J. Korecki, "Complex gamma-ray hologram: solution to twin images problem in atomic resolution imaging," Phys. Rev. Lett. **86,** 1534–1537 (2001).

63. J. P. Brody, P. Yager, R. E. Goldstein, and R. H. Austin, "Biotechnology at low Reynolds numbers," Biophys. J. **71,** 3430–3441 (1996).
64. J. Yang, Y. Huang, X. B. Wang, F. F. Becker, and P. R. C. Gascoyne, "Cell separation on microfabricated electrodes using dielectrophoretic/gravitational field flow fractionation," Anal. Chem. **71,** 911–918 (1999).
65. A. Hatch, A. E. Kamholz, K. R. Hawkins, M. S. Munson, E. A. Schilling, B. H. Weigl, and P. Yager, "A rapid diffusion immunoassay in a *T*-sensor," Nat. Biotechnol. **19,** 461–465 (2001).